Dehydration, Dehydroxylation, and Rehydroxylation of Single-Walled Aluminosilicate Nanotubes

Dun-Yen Kang,[†] Ji Zang,[†] Elizabeth R. Wright,[‡] Arthur L. McCanna,[‡,§] Christopher W. Jones,[†,*] and Sankar Nair[†,*]

[†]School of Chemical & Biomolecular Engineering, Georgia Institute of Technology, 311 Ferst Drive NW, Atlanta, Georgia 30332-0100, [‡]Department of Pediatrics, Emory University and Children's Healthcare of Atlanta, 2015 Uppergate Drive NE, Atlanta, Georgia 30322, and [§]Robert P. Apkarian Integrated Electron Microscopy Core, Emory University, 1521 Dickey Drive, Atlanta, Georgia 30322

ABSTRACT Single-walled metal oxide (aluminosilicate) nanotubes are excellent candidates for addressing the long-standing issue of functionalizing nanotube interiors, due to their high surface reactivity and controllable dimensions. However, functionalization of the nanotube interior is impeded by its high surface silanol density (9.1 −OH/nm^2) and resulting hydrophilicity. Controlled dehydration of the nanotubes is critical for the success of functionalization efforts. We employ a range of solid-state characterization tools to elucidate dehydration and dehydroxylation phenomena in the nanotubes as a function of heat treatment up to 450 °C. Vibrational spectroscopy (Fourier transform infrared, FT-IR), thermogravimetric analysis-mass spectrometry (TGA-MS), nitrogen physisorption, solid-state NMR, and X-ray diffraction (XRD) reveal that a completely dehydrated condition is achieved at 250 °C under vacuum and that the maximum pore volume is achieved at 300 °C under vacuum due to partial dehydroxylation of the dehydrated nanotube. Beyond 300 °C, further dehydroxylation partially disorders the nanotube wall structure. However, a unique rehydroxylation mechanism can partially reverse these structural changes upon re-exposure to water vapor. Finally, detailed XRD simulations and experiments allow further insight into the nanotube packing, the dimensions, and the dependence of nanotube XRD patterns on the water content.

KEYWORDS: inorganic nanotubes · aluminosilicate · dehydration · dehydroxylation · rehydroxylation

Synthetic metal oxide single-walled nanotubes (SWNTs) can be expected to possess a number of interesting and unique properties and are of interest in a variety of applications, such as molecular separation, chemical sensing, catalysis, and photonics.[1−6] Although the number of such SWNT materials is not yet extensive, an attractive aspect of these materials is that they can be fabricated by liquid-phase synthesis under moderate conditions, often hydrothermal or solvothermal conditions.[1] More specifically, a particular metal oxide (aluminosilicate) SWNT, which is a synthetic version of the nanotubular mineral imogolite,[7−9] has attracted substantial interest in recent years. This SWNT consists of a tubular aluminum(III) hydroxide layer on the outer surface with pendant silanol groups on the inner surface (Figure 1a). Its structure and dimensions have been studied using a number of techniques, such as electron diffraction, solid-state NMR, transmission electron microscopy (TEM), X-ray diffraction (XRD), and dynamic light scattering (DLS).[9−13] Additionally, the proposed mechanisms of single-walled metal oxide nanotube growth[10,14−17] allow several possible ways of controlling the monodispersity, composition, and structure of the nanotube product.

A long-standing issue in nanotube science and engineering is the modification (functionalization) of SWNT surfaces. Modification of the inner or outer surface of the nanotube with functional entities would greatly expand their properties and applications. For example, an outer-surface modification could increase the compatibility with solid- or liquid-phase materials, whereas an inner-surface modification would be advantageous for shape-/size-selective separations and catalysis. Diverse approaches for outer-surface modification of carbon nanotubes have been reported.[18−20] On the other hand, the modification of the inner wall of carbon nanotubes is much more difficult[20,21] due to the low reactivity of the inner wall as well as potential steric and transport limitations in delivering the functional entities to the desired sites in the nanotube. On the other hand, the surfaces of aluminosilicate SWNTs can be expected to resemble those of metal oxide/hydroxide and silicate materials and thus are more amenable to surface modification. The aluminosilicate SWNTs contain silanol (Si−OH) groups on the inner surface and hence can potentially be functionalized in a manner analogous to the well-known techniques for functionalization of mesoporous and microporous silicas.[22−29]

*Address correspondence to sankar.nair@chbe.gatech.edu (S.N.), cjones@chbe.gatech.edu (C.W.J.).

Received for review May 31, 2010 and accepted July 27, 2010.

Published online August 4, 2010. 10.1021/nn101211y

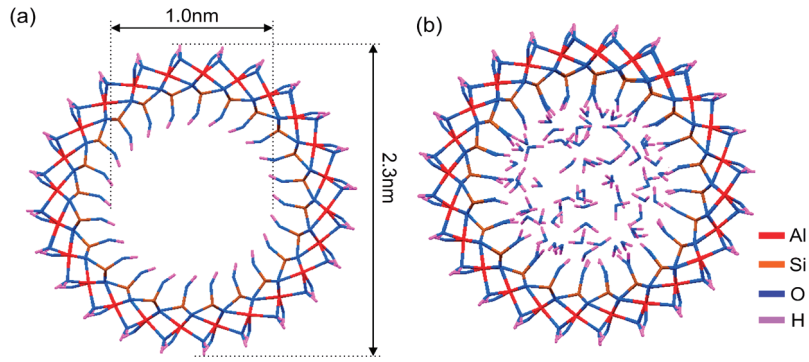

Figure 1. (a) Cross-section of single-walled aluminosilicate nanotube. (b) Example of a model of the hydrated SWNT, with 14 wt % of water physisorbed in the SWNT at ambient conditions.

The capability to control the chemistry of the inner surface of the aluminosilicate SWNTs thus has significant implications for nanotube science and engineering. There have been several reports on the outer-surface modification of single-walled aluminosilicate nanotubes.[2,30−34] However, as in the case of carbon nanotubes, inner-wall modification is much more difficult, and no convincing results suggesting inner-wall functionalization have been published. We hypothesize that the extraordinarily high surface silanol density of the inner wall (∼9.1 −OH/nm^2)[35] makes the material highly hydrophilic at ambient conditions[36,37] (Figure 1b). The strong binding of water molecules to the inner wall may hinder functionalization of the surface.

Therefore, a comprehensive knowledge of dehydration and subsequent dehydroxylation phenomena (due to condensation of hydroxyls) on the SWNT surface is critical for accessing reactive surface sites and for creating a new class of inner-wall functionalized SWNT materials. Previous studies have reported on the dehydration, dehydroxylation, and pore collapse in these SWNTs *via* solid-state NMR,[38,39] infrared spectroscopy (IR),[35] thermogravimetric analysis (TGA),[38] and X-ray diffraction (XRD).[13,35,40] However, they reach varying conclusions on many issues, for instance the heat treatment temperature required to completely dehydrate the inner wall and the temperature required for nanotube collapse. Previous studies have proposed dehydroxylation models in the absence of definitive supporting evidence. Furthermore, a quantitative study on the pore volume of the SWNT in different dehydrated and dehydroxylation conditions—a prerequisite for inner-wall modification studies—is still lacking. Here, we report a systematic qualitative and quantitative investigation of dehydration and dehydroxylation phenomena in aluminosilicate SWNTs over a wide temperature range of 25−450 °C. The structure and composition of the SWNT are assessed by a combination of techniques including *in situ* XRD, FTIR, NMR, TGA-MS, and N_2 physisorption. Based upon our results, a quantitative model is proposed for the dehydration and dehydroxylation phenomena occurring in the SWNT upon heat treatment. Furthermore, a unique rehydroxylation phenomenon that occurs in the dehydrated SWNT upon re-exposure to water is elucidated. As a result, this study leads to the preparation of a range of well-characterized heat treated materials amenable to inner-wall surface functionalization.

RESULTS AND DISCUSSION

TGA-MS. We first investigated SWNT dehydration and dehydroxylation phenomena by TGA-MS (Figure 2). According to the TGA and differential TGA curves, there are two pronounced weight losses at around 100 and 350 °C. These can be clearly assigned to dehydration and dehydroxylation, respectively. Simultaneously, the molecular weight channels 17 (corresponding to OH) and 18 (H_2O) in the mass spectrum showed two sets of concurrent peaks. The ratio of the integrated ionic current of channel 17 and 18 is around 0.25. These observations represent a well-known signature of water molecules,[41] and it is therefore clear that water molecules leave the nanotube during the entire measurement (25−700 °C). Furthermore, the trends of both ionic current channels agree with the differential TGA curve. Therefore, we can conclude that the SWNT dehydration is complete by about 250 °C, and the subsequent dehydroxylation reaches its maximum rate at about 340 °C.

Solid-State NMR. ^{1}H NMR is an excellent probe of the hydrogen environment in the SWNTs. Our ^{1}H NMR investigation is summarized in Figure 3. Sample NT25 is the original SWNT sample, NT25v is the same sample after degassing at room temperature under vacuum, and samples NT100−NT400 represent samples heat treated at the corresponding temperatures (100−400 °C). NT400r represents the rehydrated sample. Two peaks are observed in the spectra (Figure 3a): the peak between 4−6 ppm is assigned to protons from physisorbed water in the pore of the SWNT, whereas the peak at ∼1.8 ppm is assigned to the isolated hydroxyl groups.[42−44] For samples containing a significant amount of physisorbed water (NT25, NT25v, and NT400r), the NMR signal from water dominates the spectra. On the other hand, for 'anhydrous' samples, such as NT200,

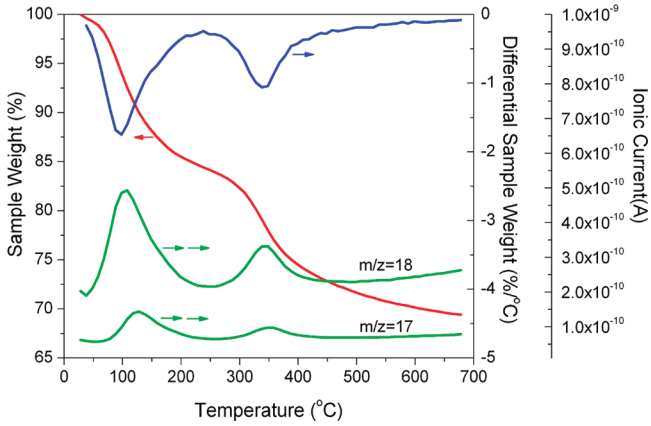

Figure 2. TGA, differential TGA, and TGA/MS ionic current traces. The ratio of ionic current between channels m/z = 18 and 17 clearly indicates that both weight losses from SWNT correspond to water molecules leaving the pores.

NT300 and NT400, the spectra are dominated by the NMR signal from isolated hydroxyl groups. A clear transition region, wherein the two peaks are of similar magnitude, is observed in the sample NT100. Furthermore, the above peak assignment can be further confirmed by the larger spectral region including spinning side bands, as summarized in Figure 3b. Previous studies suggest that the relative intensity of the central band and the spinning side band in ^{1}H solid-state NMR spectra strongly correlates to the concentration and mobility of the protons in the system.[45−48] A higher proton concentration and mobility lead to a higher intensity of the central band relative to the spinning side band. There is a monotonic increase of the relative intensities of the spinning side band and the central band from sample NT25 to NT 400v, when the SWNT sample undergoes dehydration and subsequent dehydroxylation. This observation is due to two factors: the loss of protons during heat-treatment and the loss of more mobile protons present in physisorbed water (in comparison to protons from hydroxyl groups) during dehydration.[48]

Direct- (DP) and cross- (CP) polarizations ^{29}Si NMR were then used to provide a molecular-level understanding of the interior wall structure of the SWNT during heat treatment (Figure 4a and b). In the case of CP-NMR, the signal is enhanced by the presence of protons in proximity to the silicon atoms.[49] In the original SWNT sample (NT25), only one peak located at −79 ppm is seen and assigned to Q^3(6Al), in good agreement with the study of Frost *et al.*[12] In the heat-treated samples a second, broader peak around −90 ppm is observed, its intensity being relatively insignificant for NT100−NT300 but becoming prominent for NT400. This peak was rationalized in previous works as a structural transformation from imogolite (SWNT) into a nontubular material called allophane, based upon the similarity of the NMR spectrum to that of allophane.[38,50] However, the transformation of tubular imogolite into nontubular allophane would be expected to involve drastic and irreversible morphological and structural changes in the ^{27}Al NMR spectra, vibrational spectra, XRD patterns, and N_2 physisorption isotherms. Since such irreversible and drastic changes are not observed (as discussed below), and considering the fact that the inner wall of the imogolite SWNT and allophane have a very similar silanol structure,[51,52] it is more appropriate to assign the broad peak at −90 ppm to the condensation of adjacent silanols, thus leading to a transformation of the Si coordination environment from Q^3(6Al) into Q^4(6Al). The latter is more shielded than Q^3(6Al)[53,54]

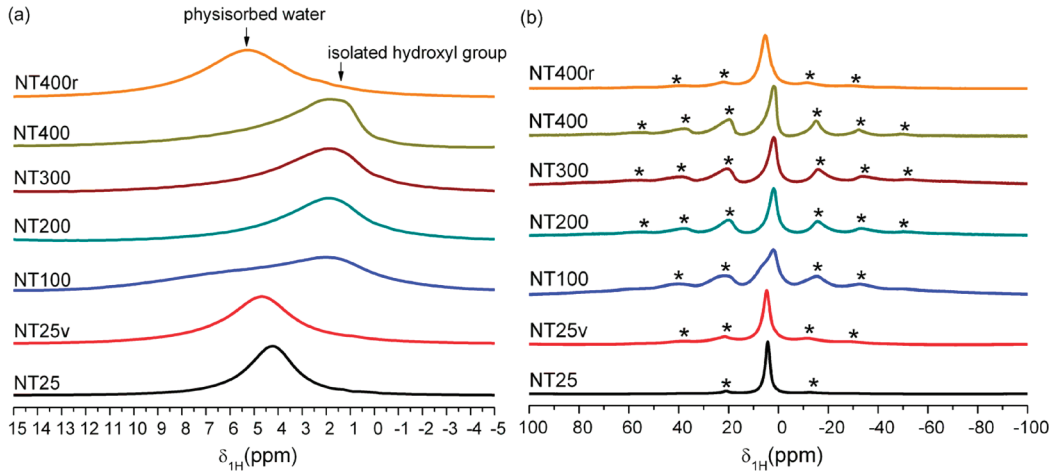

Figure 3. (a) ^{1}H NMR for the SWNT sample in different pretreated conditions. Sample NT25 is the original SWNT sample, NT25v is the same sample after degassing at room temperature under vacuum, and samples NT100−NT400 represent samples heat treated at the corresponding temperatures (100−400 °C). NT400r represents the rehydrated sample. (b) A larger spectral region of ^{1}H NMR including spinning side bands, denoted by asterisks (*), for the SWNT sample heat treated at different temperatures.

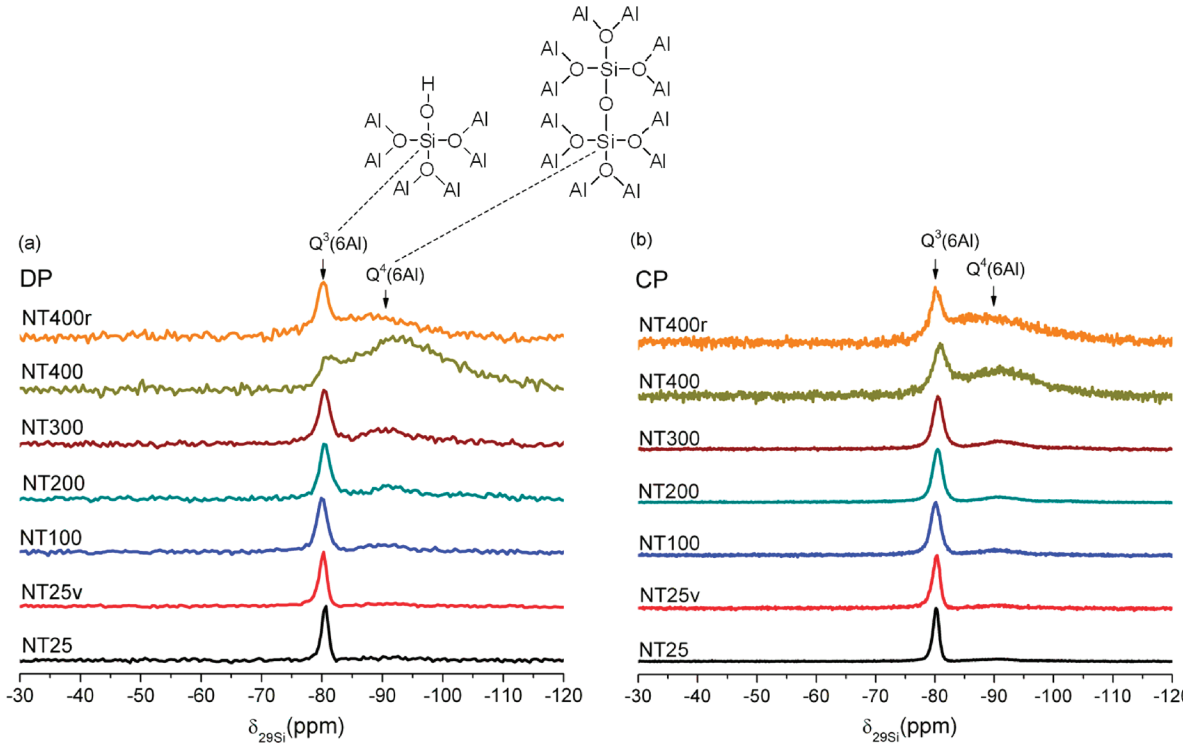

Figure 4. (a) ^{29}Si direct-polarized (DP) NMR and (b) ^{29}Si cross-polarized (CP) NMR for SWNT samples heat treated at different temperatures.

and is well-known to show an upfield chemical shift. Furthermore, the CP-NMR spectra show a more pronounced Q^3(6Al) peak in relation to the Q^4(6Al) peak. This is clear due to the enhancement of the former peak by a proximal proton coming from the silanol group, whereas this is not possible for the Q^4(6Al) signal from fully condensed silanols. When the SWNT sample is rehydrated (NT400r), a distinct change (in comparison to NT400) occurs. The Q^3(6Al) signal dominates the spectrum again, as in the samples NT25−NT300. This is clear evidence of a rehydroxylation phenomenon, wherein most of the condensed Q^4(6Al) silicon atoms in NT400 are transformed (by hydrolysis) back into silanols when the anhydrous dehydroxylated sample is re-exposed to moisture. Note that there is no obvious difference between the DP- and CP-NMR spectra for NT400r, since the protons from the hydroxyl group can enhance the Q^3(6Al) signal, whereas the protons from physisorbed water are able to enhance the Q^4(6Al) signal. Regarding our use of the Q^3(6Al) and Q^4(6Al) labels, the first ^{29}Si NMR study on imogolite nanotubes[12] uses the notation of Q^3(3Al) for the Si atoms. The terminology of Q^n(*n*Al) is also commonly used in identifying aluminum substitution for tetrahedral silica framework for zeolites.[53] However, the framework of imogolite is different from zeolites due to the three coordinated oxygen connecting the tetrahedral silicon and two octahedral aluminums. To avoid any confusion, we have therefore renamed the silica coordination as Q^3(6Al) and Q^4(6Al).

Based on the initial chemical composition of the inner wall, we can quantitatively summarize the dehydroxylation and rehydroxylation phenomena of the SWNT interior in the following scheme:

$$SiO_{2.5}H \underset{\text{re-exposed to moisture}}{\overset{\text{heat}}{\rightleftharpoons}} (1 - x)SiO_{2.5}H + xSiO_2 + 0.5xH_2O \quad (1)$$

where $0 \leq x \leq 1$. We obtained the value of x from the ratio of the integrated Q^3(6Al) and Q^4(6Al) peak areas in DP spectra. The value of $x = 0.04$, 0.20, and 0.73 for NT25, NT300, and NT400 respectively, corresponding to the increasing condensation of silanols upon heat treatment. Upon rehydroxylation to yield sample NT400r, the value of x falls to 0.29.

While ^{29}Si NMR elucidates structural changes in the interior of the SWNT, ^{27}Al NMR (Figure 5) gives information on structural changes occurring in the nanotubular gibbsite (aluminum hydroxide) layer comprising its outer surface. The peak at 4 ppm is assigned to the octahedrally coordinated aluminum, which is the only type of aluminum present in the purified original SWNT material (NT25).[50] The spectra remain unchanged until NT400, wherein a broad shoulder is observed. When the anhydrous dehydroxylated SWNT sample is rehydroxylated (NT400r), the shoulder further resolves into clear peaks at 30 and 60 ppm. The peak at 60 ppm is clearly assigned to tetrahedral aluminum,[55,56] whereas there are several possible assignments for the peak at 30 ppm. Previous studies suggest that the peak in the range of 20−50 ppm can be reasonably assigned to distorted tetrahedral aluminum,[57,58] distorted octahedral

aluminum,[55] or penta-coordinated aluminum.[55,56,59,60] In the following discussion, we assigned the peak at 30 ppm to penta-coordinated aluminum in analogy to the structural transformation of gibbsite under calcination.[60] Our detailed study shows that it is appropriate to attribute the penta-coordinate Al to local changes in the structure of the SWNT due to (reversible) condensation of a fraction of the silanol groups and to a concomitant (irreversible) decrease in the coordination environment of a fraction of the aluminum atoms.

Based upon the ^{27}Al spectra, we are able to propose a model for the (irreversible) SWNT dehydroxylation at the outer surface:

$$Al_2O_{4.5}H_3 \xrightarrow{\text{heat}} (1 - y - z)Al_2O_{4.5}H_3 + 2yAlO_{4/3} + 2zAlO_{5/3} + 1.5(y + z)H_2O \quad (2)$$

where $0 \leq (y,z) \leq 1$, and $AlO_{4/3}$ and $AlO_{5/3}$ represent tetrahedral and penta-coordinated aluminum, respectively. We performed a quantitative analysis for the values of y and z in a manner similar to our analysis of the ^{29}Si NMR spectra. For example, we obtained $(y,z) = (0,0)$ and (0.06, 0.14) for NT25 and NT400, respectively, reflecting the conversion of octahedral aluminum during heat treatment. On the other hand, the rehydroxylated sample NT400r gives $(y,z) = (0.09, 0.06)$. However, it must be cautioned that the quantitative interpretation of the ^{27}Al NMR spectrum[58,61] for sample NT400 is less reliable than that for NT400r, since it has been suggested that reliable quantitative analysis of ^{27}Al NMR spectra should be derived from fully hydrated samples,[62,63] whereas NT400 is completely dehydrated. Specifically, differences in coordination environment and hydration level may affect the intensity of ^{27}Al signals due to its quadrupole moment and thus may contribute to the better resolution of the NMR signals from penta-coordinated and tetrahedral aluminum in sample NT400r as compared to NT400.

Nitrogen Physisorption. N_2 physisorption measurements for SWNT samples heat treated at different temperatures were performed to investigate how dehydration, dehydroxylation, and structural transformation affects the SWNT pore volume (Figure 6). The original SWNT sample (NT25) did not show a significant pore volume due to occupation of the pores by physisorbed water. The physisorption isotherms from the SWNT sample degassed at ambient conditions (NT25v) and heat treated at 100 °C (NT100) show characteristics of an IUPAC Type II isotherm (a detailed view of the isotherms for samples NT25v and NT100 is presented in the Supporting Information),[64] which indicates nonporosity due to pore blocking by physisorbed water. In contrast, as the SWNT samples become more dehydrated (NT200 and NT300), the shape of the isotherm transforms to an IUPAC Type I, distinctly suggesting activation of the porosity of the SWNT interior. The monotonic increase in

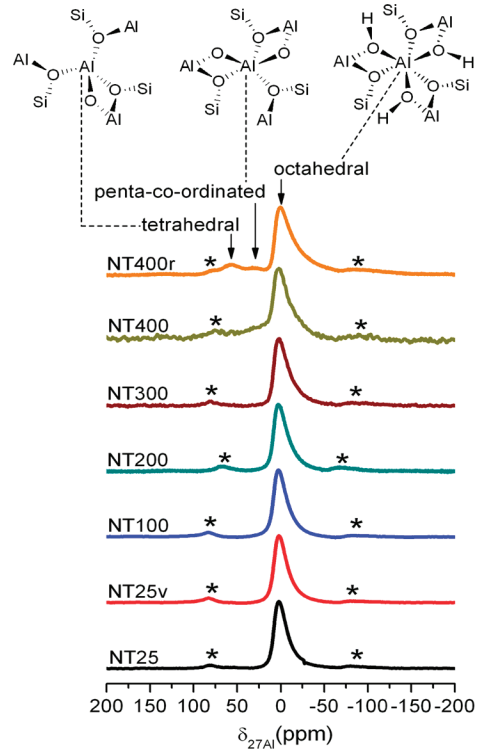

Figure 5. ^{27}Al NMR spectra of SWNT samples heat treated at different temperatures. Asterisks (*) denote the spinning side band artifacts.

the pore volume from NT25 to NT200 is due to SWNT dehydration and from NT200 to NT 300 by dehydroxylation, in qualitative agreement with TGA-MS and FTIR studies discussed later in this report.

However, a pore volume decrease is observed as the heat treatment temperature goes from 300 to 400 °C. This phenomenon could be rationalized by partial pore blocking caused by the structural transformations accompanying dehydroxylation. Even though the wall structure of NT400 is likely to be partially damaged or disordered, the isotherm still shows high microporosity. The further drop in pore volume for NT400r, in comparison to NT400, is presumably due to the decrease in pore volume due to the reconstitution of a substantial number of silanol groups as well as the reoccupation of the SWNT pores with some amount of strongly physisorbed water. However, a study of SWNT structural deformation accompanied by pore collapse at high temperature ($T > 400$ °C) is beyond the scope of the present paper. This aspect has been studied by Mackenzie *et al.*[38]

FT-IR. The IR absorbance spectra of samples heat treated and degassed at different temperatures are summarized in Figure 7a. The absorption at 1630 cm^{-1} is well-known to represent the scissoring mode of physisorbed water. The rather broad absorption in the 2800−3800 cm^{-1} region is due to various stretching vibrations of O−H groups in the material: silanols at the inner surface, bridging Al−(OH)−Al groups at the outer surface, physisorbed water, and hydrogen-bonding interactions between these species. Due to the intrinsically limited reso-

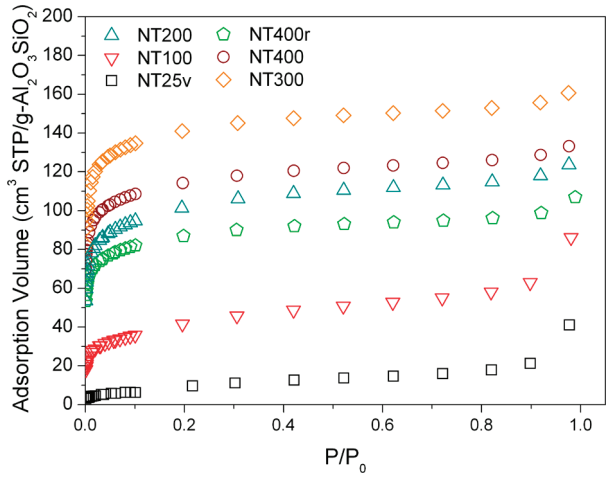

Figure 6. N_2 physisorption isotherms of SWNT samples prepared by different heat treatment conditions.

lution of solid-state IR spectra, an assignment of the roles of these individual vibrational species is not possible. However, since all IR spectra were collected *in situ* on the same sample, a quantitative estimate of the amount of water and hydroxyl groups can be made on the basis of the integrated areas under the two respective absorbance peaks. Figure 7b shows the concentration of physisorbed water in the different samples, normalized by the water concentration in the SWNT sample at ambient conditions (NT25). This result confirms that most (~90%) of the physisorbed water is removed by vacuum heat treatment up to 150 °C and that the SWNT sample is completely dehydrated by 250 °C. The hydroxyl concentration in samples NT250−NT450, normalized by the hydroxyl concentration of the "baseline" dehydrated sample (NT250), is also shown in Figure 7b. It is suggested that around 30% of the hydroxyl groups (~2.7 −OH/nm^2) survive at 450 °C. Furthermore, FT-IR spectra of the as-synthesized SWNT and SWNT treated at 400 °C, over the entire 400−4000 cm^{-1} region, are presented in the Supporting Information. There are no drastic peak shifts, appearances, or disappearances observed in the "material fingerprint" region (400−1400 cm^{-1}).

XRD Measurements and Simulations. To complete our study of the SWNT structure during dehydration and to investigate the packing of the SWNTs in the solid sample, we performed *in situ* XRD measurements on SWNT samples heat treated at various temperatures. Our experimental results (Figure 8a and b) show a substantial intensity increase of the first peak at 3.9° 2θ upon dehydration from NT25 to NT250. On the other hand, the fourth peak at 13.3° 2θ remains constant in intensity. Beyond a heat treatment temperature of 250 °C, there is a monotonic decrease in the intensity of the first peak due to the structural transformation and the partial pore collapse, which are also suggested in the nitrogen physisorption isotherms.

A detailed XRD simulation study was performed in order to extract reliable structural information during nanotube dehydration. In a previous work,[10] the XRD patterns of SWNT film samples were qualitatively interpreted in terms of Bragg diffraction from a crystalline bundle of nanotubes. Several later studies investigated the XRD patterns more quantitatively.[65−67] In particular, a more accurate model of the XRD patterns can be obtained by considering diffraction from small SWNT bundles (each composed of only a few nanotubes). However, a good agreement between experimental and simulated XRD patterns has not been achieved due to the effects of several parameters, such as the number of SWNTs in a single bundle, the number of gibbsite structural units in the SWNT circumference, internanotube distance, and the degree of hydration. We performed a systematic XRD simulation study on both dehydrated and hydrated SWNTs to achieve the best fit of the simulated XRD patterns. The details of the XRD simulation model and results are presented in the Supporting Information. We summarize the main results here.

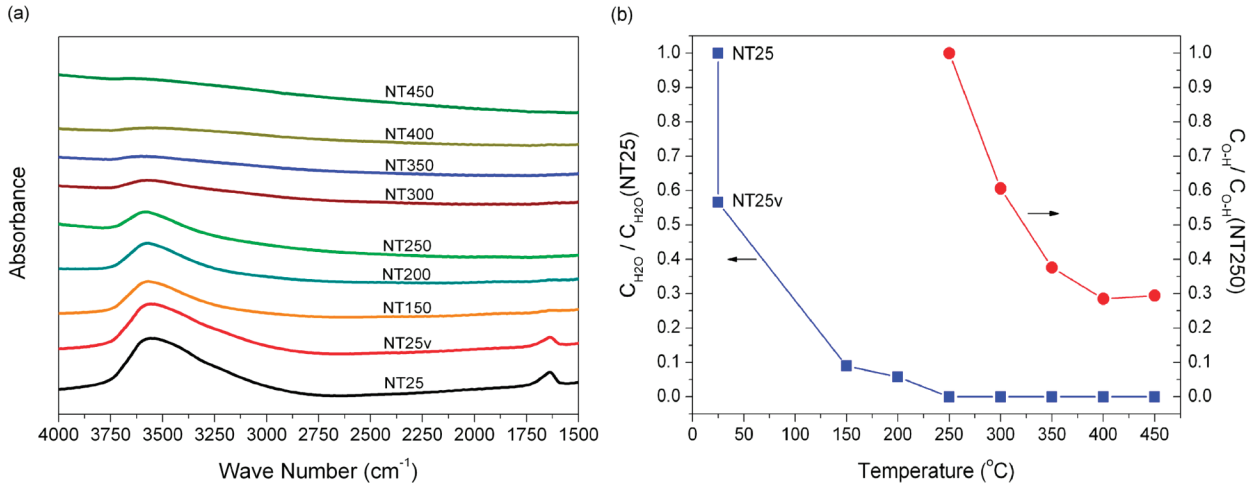

Figure 7. (a) FT-IR spectra of heat-treated SWNT samples. All spectra are plotted to scale and stacked in a vertical series. (b) Normalized physisorbed water and hydroxyl group concentrations in the SWNT at different heat treatment temperatures as calculated from FT-IR spectra.

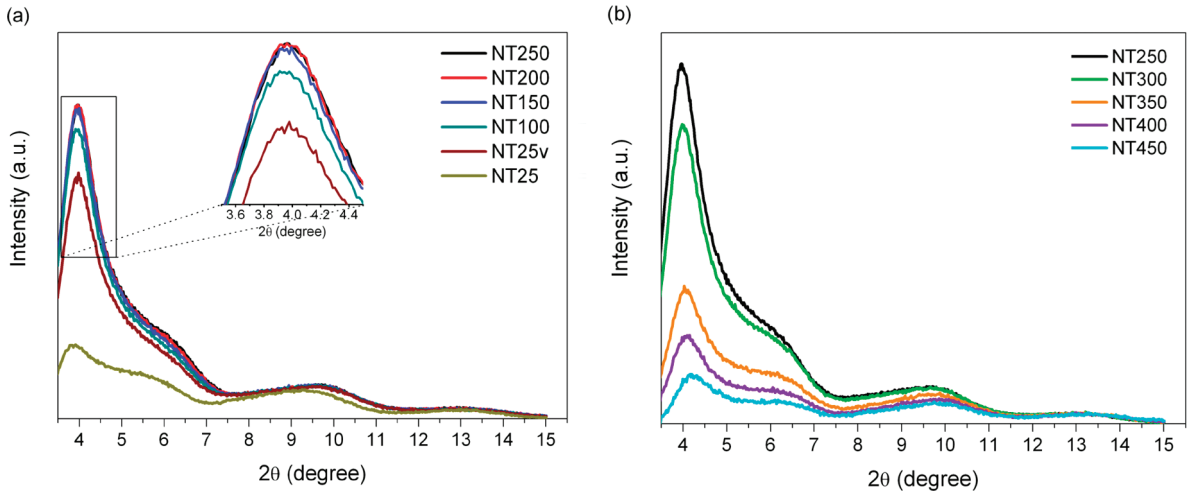

Figure 8. ***In situ*** **XRD patterns of the SWNT sample: (a) from room temperature to 250 °C, and (b) from 250−450 °C. All patterns are plotted to scale.**

After extensive parameter variation studies (Supporting Information), it was found that the best agreement with the experimental XRD patterns could be obtained by either a 2 × 2 bundle of SWNTs with a monoclinic packing angle of 75° or a triangular arrangement of 3 SWNTs with a hexagonal packing angle of 60°. Although a hexagonal packing is intuitively assumed in many studies, a monoclinic packing angle of ~78° has also been proposed previously[10,69] based on circular dichroism and XRD measurements. Another important parameter is the number of replicating gibbsite units (N_u) in the SWNT circumference. Several recent computational studies[66,70,71] employing quantum chemistry or classical force field techniques suggest the thermodynamically favored value of $N_u = 12$. However, the XRD simulations show that models with $N_u = 14$ agree somewhat better with experimental data. It is not possible to conclusively identify the exact value of N_u based upon the XRD patterns. Hence, in Figure 9 we depict simulation results for both values of N_u and for both "best fit" packing models.

In all four cases, the intensity of the first peak strongly correlates with the amount of physisorbed water, whereas the intensity of the fourth peak stays constant. Thus, the effect of hydration on the XRD patterns of the present SWNTs is analogous to the effect of C_{60} buckyballs in the pores of carbon nanotubes (*i.e.*, "peapod" structures)[72−74] on the XRD patterns of carbon nanotube bundles. Therefore, we can quantitatively correlate the integrated intensity of the first peak (as obtained from the simulated XRD patterns) with the water content (Figure 10a). Strongly linear correlations are derived for all four SWNT packing models. With these correlations, we can calculate the water content of the SWNTs from the experimental XRD data (Figure 10b). The results indicate that there is ~15 wt % water physisorbed in the SWNT at ambient conditions. This is in good agreement with the TGA results (shown in Figure 10b) as well as with Monte Carlo simulation results.[37,68] However, the shape of the TGA curve cannot be directly compared to the XRD results owing to the different conditions of these experiments. The former is a dynamic water loss measurement carried out under flowing helium, whereas the XRD patterns are from samples equilibrated under vacuum.

In conclusion, the phenomenology and mechanisms of dehydration and dehydroxylation in single-walled aluminosilicate nanotubes have been evaluated comprehensively in this study. A quantitative dehydration investigation *via* Fourier transform infrared (FT-IR), thermogravimetric analysis (TGA), and X-ray diffraction (XRD) suggests that the SWNT sample contains *ca.* 15% physisorbed water under ambient conditions and becomes completely dehydrated at 250 °C. Dehydroxylation, which (reversibly) transforms Q^3(6Al) silicons into Q^4(6Al) and (irreversibly) transforms octahedral aluminum into pentacoordinated and tetrahedral aluminum, takes place beyond 250 °C as elucidated by NMR spectroscopy. A quantitative model for these processes was deduced from our investigation. A unique rehydroxylation phenomenon, which transforms condensed Q^3(6Al) silicons back into Q^4(6Al) silicons upon re-exposure to water vapor, has been found by ^{29}Si NMR and N_2 physisorption. Furthermore, N_2 physisorption and XRD show that dehydration and initial dehydroxylation lead to a high microporosity of the nanotubes, whereas dehydroxylation at 400 °C or higher leads to partial pore collapse. The SWNT reaches its maximum pore volume (~1.4 times that of the anhydrous SWNT obtained at 250 °C) at 300 °C, at which temperature about 40% dehydroxylation has also occurred, and an inner surface silanol concentration of 5.5 −OH/nm^2 exists. Hence, we conclude that heat treatment under vacuum at 250−300 °C is an optimal pretreatment condition for full dehydration and for yielding maximum pore volume, while maintaining the nanotubular structure before surface modification of the SWNT under anhydrous conditions.

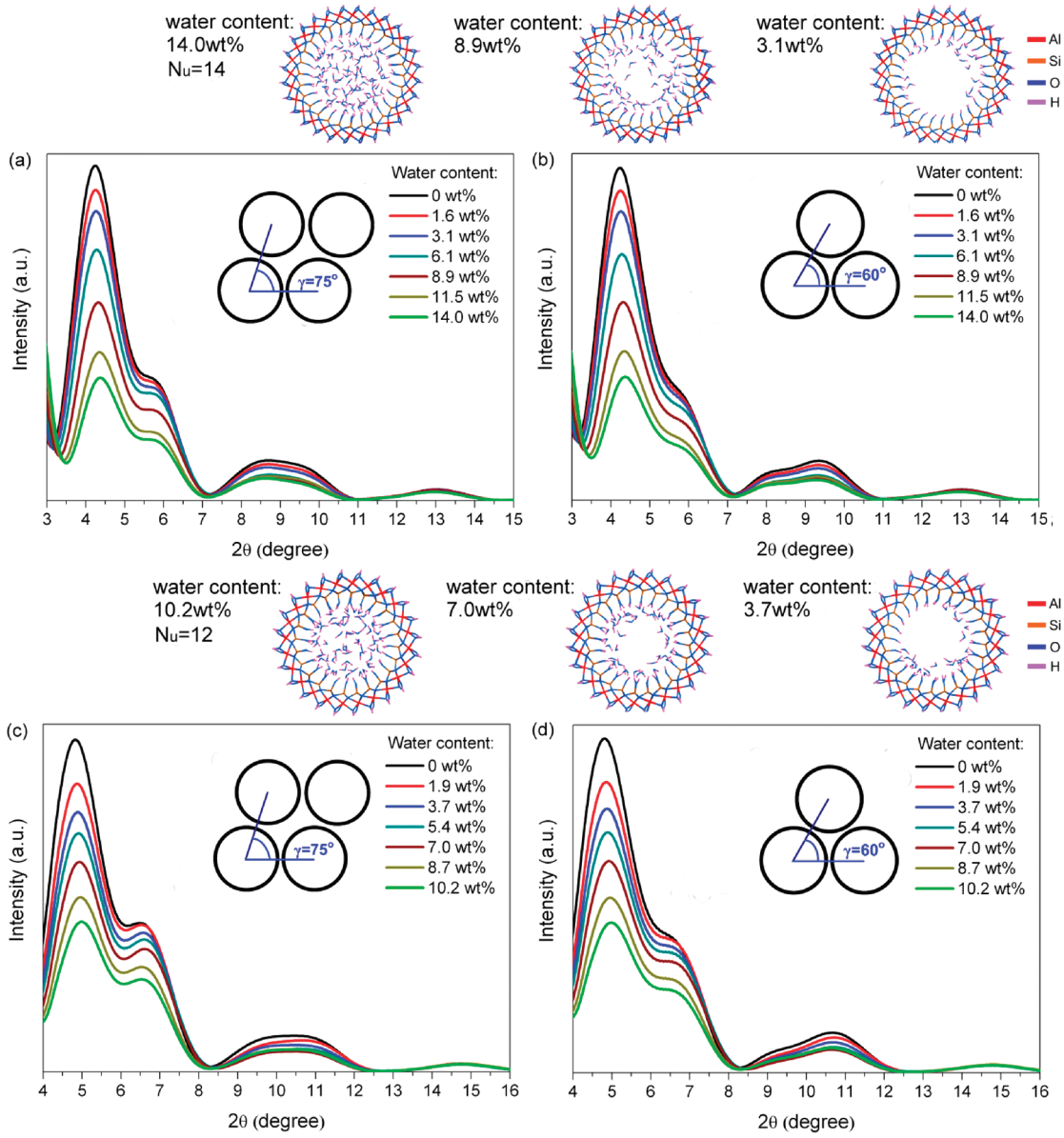

Figure 9. (a) Simulated XRD patterns of the SWNT sample with different diameters, bundle structures, and water contents: (a) $N_u = 14$, 2 × 2 bundling; (b) $N_u = 14$, triangular bundling; (c) $N_u = 12$, 2 × 2 bundling; and (d) $N_u = 12$, triangular bundling. The SWNT−water models are obtained by grand canonical Monte Carlo (GCMC) simulations (details of the GCMC simulation are included in the Supporting Information). Examples of SWNT−water models are also shown.[68]

Based on the present observations, the SWNTs can potentially be applied for molecular separation, adsorption, molecular encapsulation, and catalysis after appropriate functional groups are introduced. Finally, we show that the XRD patterns of the SWNTs at various degrees of dehydration can be quantitatively modeled and matched to experimental data. Our investigation yielded four likely models for SWNT packing and a number of gibbsite units (N_u) among the many possibilities as well as provided a quantitative correlation between the water content and the X-ray scattering intensity from the SWNT. These four possibilities will enable a more detailed investigation to ascertain the unique packing model and the exact number of gibbsite units in the SWNT circumference.

METHODS

SWNT Synthesis and Purification. Tetraethyl orthosilicate (TEOS) was mixed with aluminum-tri-*sec*-butoxide in a glovebox filled with nitrogen. The mixture was added to an aqueous 10 mM perchloric acid solution with a molar ratio Si:Al:$HClO_4$ = 1.1:2:1, under vigorous stirring at room temperature in ambient conditions for 24 h. The solution was then diluted with DI water by a factor of 3.6 and refluxed at 95 °C for 4 days. Once the temperature was brought to 95 °C, the solution turned from cloudy to clear in about 1 h. After the solution was decreased to room temperature, a 30 wt % ammonia solution was added dropwise into the product solution until gelation of the suspended nano-

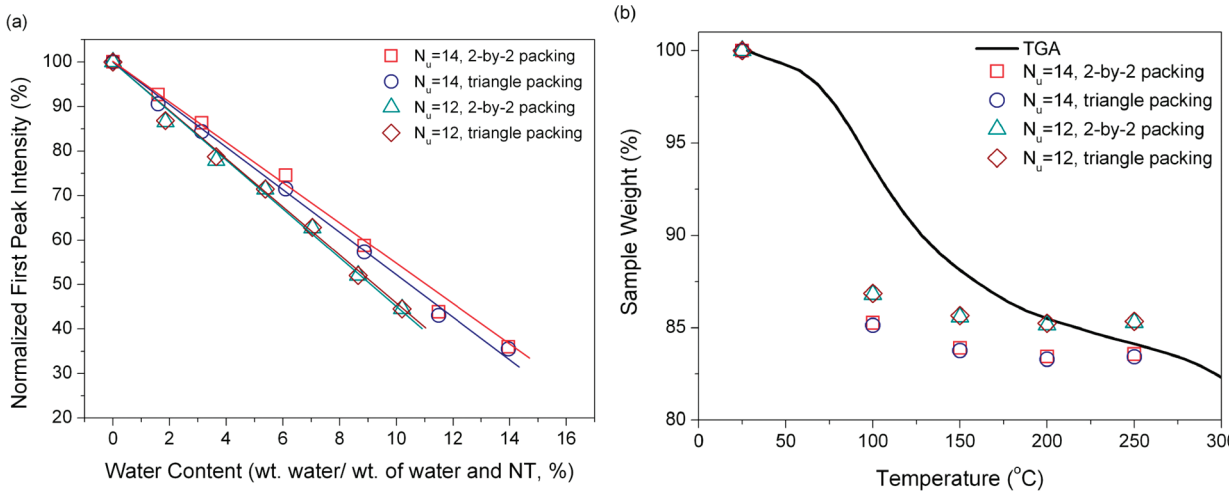

Figure 10. (a) Correlations of the first low angle peak from simulated XRD patterns versus the weight fraction of water for four sets of simulation parameters. (b) SWNT sample weight loss calculated from experimental *in situ* XRD patterns and the correlation function derived in (a). The TGA trace is also included for comparison.

tubes occurred. The gel was isolated by centrifugation at 7000 rpm for 15 min. The supernatant was discarded, and a few drops of 10 N hydrochloric acid were added to the gel, thereby redispersing the nanotubes. The resulting viscous solution was purified by dialysis against DI water for 3 days using a 15 000 Dalton membrane. The purified suspension was dried at 60 °C to obtain a powder sample of the SWNTs.

Cryo-TEM Imaging. The as-synthesized dialyzed product solution was imaged by cryo-TEM to confirm the presence of the SWNTs and to obtain clear images of these materials (Supporting Information) that cannot be obtained by conventional TEM. Four μL aliquots of single-walled metal oxide (aluminosilicate) nanotubes were applied onto glow-discharged, 200 mesh, holey carbon-coated copper grids (EMSciences, Hatfield, Pennsylvania) and flash frozen (plunge frozen) in liquid ethane using a Vitrobot Mark II system (FEI, Hillsboro, Oregon). Plunge-frozen samples were stored under liquid nitrogen until viewed in the electron microscope. Cryo-electron micrographs were collected at the Emory University Robert P. Apkarian Integrated Electron Microscopy Core using a JEOL JEM-1210 microscope operated at 100 kV. The microscope is equipped with a LaB_6 filament and a Gatan CT-3500 cold stage. Images were acquired with a Gatan UltrascanTM 2 k × 2 k charged couple device (CCD camera) (Gatan, Inc. Pleasanton, CA).

Thermogravimetric Analysis and Mass Spectroscopy (TGA-MS). These experiments were performed on a Netzsch STA449 TGA connected to a Netzsch QMS403 mass analyzer. About 20 mg of SWNT sample was heated under He in the range of 25−700 °C.

Nitrogen Physisorption. Nitrogen physisorption measurements were performed with a Micromeritics ASAP 2010 at 77 K. The nanotube sample was placed in an analysis tube, degassed, and heat treated at the desired temperature for 12 h in a 25 mTorr vacuum before each measurement. Heat treatments at higher temperatures, *e.g.*, 300−400 °C, were conducted in a separate 15 mTorr vacuum line for 5 h, and the sample was then transferred into the analysis tube in a nitrogen glovebox before degassing and physisorption measurements. To obtain a rehydrated nanotube sample, the sample after heat treatment at 400 °C was cooled to room temperature and allowed to equilibrate in contact with saturated water vapor for 12 h. In contrast to the other characterization methods reported here (which characterize the rehydrated sample directly), physisorption measurements were made on the rehydrated sample only after it was degassed under vacuum at 250 °C.

Solid-State NMR. The nanotube sample for solid-state NMR experiments was first placed in a flask connected to a 15 mTorr vacuum line and heat treated at the desired temperature for 5 h. The rehydrated sample was treated as described above. The treated sample was transferred to a nitrogen drybox and packed into a 7 mm rotor capped with one O-ring cap. ^{1}H, ^{27}Al, and ^{29}Si MAS NMR experiments were carried out on a Bruker DSX 300 spectrometer at frequencies of 276.2, 78.1, and 59.6 MHz, respectively. For ^{1}H MAS NMR studies, the sample was spun at 5 kHz. A single pulse of $\pi/2$ and a repetition time of 4 s was used. The sample was spun at 5−6 kHz for ^{27}Al MAS NMR experiments, for which a single pulse of $\pi/6$ and a repetition time of 0.1 s were used. For ^{29}Si MAS NMR, DP and CP measurements were performed with repetition times of 10 and 5 s, respectively, with a $\pi/2$ single pulse and a 5 kHz spinning rate. The chemical shifts of ^{27}Al was referenced to $AlCl_3$ and ^{1}H and ^{29}Si to 3-(trimethylsilyl)-1-propanesulfonic acid sodium salt.

FT-IR. A 2 mg nanotube sample was mixed with 40 mg potassium bromide (KBr) and pressed into a pellet. The sample pellet was placed in a Harrick high-temperature cell with KBr windows. The sample pellet was heat treated under a 15 mTorr vacuum at various temperatures ranging from 25−450 °C for 5 h each. The cell was then cooled to room temperature and filled with argon before conducting FT-IR measurements. The FT-IR spectra were obtained on a Bruker IFS 66v/S spectrometer with 256 scans and a resolution of 2 cm^{-1}. Peak area integrations were performed using the OPUS 6.5 program (Bruker).

X-ray Diffraction (XRD) Measurements and Simulations. *In situ* powder XRD was performed on PAnalytical X'pert Pro diffractometer operating with a Cu Kα source. The powder sample was placed in an Anton Paar TTK 450 temperature-controlled chamber. The sample was heat treated at a desired temperature for 5 h under a vacuum of 7.5 mTorr, and high-resolution diffraction data were then rapidly collected with an X'Celerator detector scanning from 2−30° 2θ with a step size of 0.02°. XRD simulations were performed using the Reflex module of the Materials Studio 3.2 molecular simulation package (Accelrys, Inc.). A polarization factor of 0.5 was used, assuming the sample is in powder form. The instrumental broadening was accounted for by a well-known angle-independent full-width-at-half-maximum (fwhm) expression containing parameters (*U*, *V*, and *W*). The values of these three parameters ($U = 0.6787$, $V = -0.2563$, and $W = 0.03378$) were obtained by fitting the peak shape of the experimental diffraction pattern of LaB_6 (NIST) measured on the same instrument. Atomistically detailed nanotube models with various degrees of hydration were constructed by adapting techniques described in our recent simulation studies of water adsorption and transport in the aluminosilicate SWNTs.[37,68] The XRD simulations were carried out with atomistically detailed models of nanotube bundles containing various numbers of nanotubes in different bundling patterns (hexagonal, monoclinic, and orthogonal).

Acknowledgment. This work was supported by the ConocoPhillips Company. The authors also acknowledge Dr. K. S. Walton (Georgia Tech) for access to TGA-MS instrumentation and Dr. J. Leisen (Georgia Tech) and Dr. K. C. McCarley (ConocoPhillips) for useful discussions.

Supporting Information Available: Cryo-TEM images, detailed N_2 physisorption isotherms, and FT-IR spectra of the SWNTs; equations used for simulating the SWNT X-ray diffraction patterns; details of the GCMC simulation model for the SWNT/water system; detailed XRD simulation results for bundles of dehydrated SWNTs; and analysis of the effects of nanotube diameter, intertubular distance, packing angle, bundle size, and unit cell dimensions on the XRD patterns.This material is available free of charge *via* the Internet at http://pubs.acs.org.

REFERENCES AND NOTES

1. Rao, C. N. R.; Govindaraj, A. Synthesis of Inorganic Nanotubes. *Adv. Mater.* **2009**, *21*, 4208–4233.
2. Yamamoto, K.; Otsuka, H.; Takahara, A. Preparation of Novel Polymer Hybrids from Imogolite Nanofiber. *Polym. J.* **2007**, *39*, 1–15.
3. Tenne, R.; Seifert, G. Recent Progress in the Study of Inorganic Nanotubes and Fullerene-Like Structures. *Annu. Rev. Mater. Res.* **2009**, *39*, 387–413.
4. Son, S. J.; Bai, X.; Lee, S. B. Inorganic Hollow Nanoparticles and Nanotubes in Nanomedicine. Part 1. Drug/Gene Delivery Applications. *Drug Discovery Today* **2007**, *12*, 650–656.
5. Cheng, F. Y.; Chen, J. Storage of Hydrogen and Lithium in Inorganic Nanotubes and Nanowires. *J. Mater. Res.* **2006**, *21*, 2744–2757.
6. Goldberger, J.; Fan, R.; Yang, P. D. Inorganic Nanotubes: A novel Platform for Nanofluidics. *Acc. Chem. Res.* **2006**, *39*, 239–248.
7. Wada, K.; Yoshinag, N. Structure of Imogolite. *Am. Mineral.* **1969**, *54*, 50–71.
8. Farmer, V. C.; Smith, B. F. L.; Tait, J. M. Stability, Free-Energy and Heat of Formation of Imogolite. *Clay Miner.* **1979**, *14*, 103–107.
9. Wada, S. I.; Eto, A.; Wada, K. Synthetic Allophane and Imogolite. *J. Soil Sci.* **1979**, *30*, 347–352.
10. Mukherjee, S.; Bartlow, V. A.; Nair, S. Phenomenology of the Growth of Single-Walled Aluminosilicate and Aluminogermanate Nanotubes of Precise Dimensions. *Chem. Mater.* **2005**, *17*, 4900–4909.
11. Farmer, V. C.; Fraser, A. R.; Tait, J. M. Synthesis of Imogolite - Tubular Aluminum Silicate Polymer. *J. Chem. Soc. Chem. Commun.* **1977**, 462–463.
12. Barron, P. F.; Wilson, M. A.; Campbell, A. S.; Frost, R. L. Detection of Imogolite in Soils Using Solid-State 29Si NMR. *Nature* **1982**, *299*, 616–618.
13. Vandergaast, S. J.; Wada, K.; Wada, S. I.; Kakuto, Y. Small-Angle X-ray-Powder Diffraction, Morphology, and Structure of Allophane and Imogolite. *Clays Clay Miner.* **1985**, *33*, 237–243.
14. Yang, H. X.; Wang, C.; Su, Z. H. Growth Mechanism of Synthetic Imogolite Nanotubes. *Chem. Mater.* **2008**, *20*, 4484–4488.
15. Wilson, M. A.; Lee, G. S. H.; Taylor, R. C. Tetrahedral Rehydration during Imogolite Formation. *J. Non-Cryst. Solids* **2001**, *296*, 172–181.
16. Bursill, L. A.; Peng, J. L.; Bourgeois, L. N. Imogolite: an Aluminosilicate Nanotube Material. *Philos. Mag. A* **2000**, *80*, 105–117.
17. Hu, J.; Kamali Kannangara, G. S.; Wilson, M. A.; Reddy, N. The Fused Silicate Route to Protoimogolite and Imogolite. *J. Non-Cryst. Solids* **2004**, *347*, 224–230.
18. Singh, S.; Kruse, P. Carbon Nanotube Surface Science. *Int. J. Nanotechnol.* **2008**, *5*, 900–929.
19. Grossiord, N.; Loos, J.; Regev, O.; Koning, C. E. Toolbox for Dispersing Carbon Nanotubes into Polymers to Get Conductive Nanocomposites. *Chem. Mater.* **2006**, *18*, 1089–1099.
20. Lin, T.; Bajpai, V.; Ji, T.; Dai, L. M. Chemistry of Carbon Nanotubes. *Aust. J. Chem.* **2003**, *56*, 635–651.
21. Kyotani, T.; Nakazaki, S.; Xu, W. H.; Tomita, A. Chemical Modification of the Inner Walls of Carbon Nanotubes by HNO_3 Oxidation. *Carbon* **2001**, *39*, 782–785.
22. Kupiec, K.; Konieczka, P.; Namiesnik, J. Characteristics, Chemical Modification Processes as well as the Application of Silica and its Modified Forms. *Crit. Rev. Anal. Chem.* **2009**, *39*, 60–69.
23. McMorn, P.; Hutchings, G. J. Heterogeneous Enantioselective Catalysts: Strategies for the Immobilisation of Homogeneous Catalysts. *Chem. Soc. Rev.* **2004**, *33*, 108–122.
24. De Vos, D. E.; Dams, M.; Sels, B. F.; Jacobs, P. A. Ordered Mesoporous and Microporous Molecular Sieves Functionalized with Transition Metal Complexes as Catalysts for Selective Organic Transformations. *Chem. Rev.* **2002**, *102*, 3615–3640.
25. Sayari, A.; Hamoudi, S. Periodic Mesoporous Silica-Based Organic - Inorganic Nanocomposite Materials. *Chem. Mater.* **2001**, *13*, 3151–3168.
26. Ying, J. Y.; Mehnert, C. P.; Wong, M. S. Synthesis and Applications of Supramolecular-Templated Mesoporous Materials. *Angew. Chem., Int. Ed.* **1999**, *38*, 56–77.
27. Cheng, C. H.; Bae, T. H.; McCool, B. A.; Chance, R. R.; Nair, S.; Jones, C. W. Functionalization of the Internal Surface of Pure-Silica MFI Zeolite with Aliphatic Alcohols. *J. Phys. Chem. C* **2008**, *112*, 3543–3551.
28. Hicks, J. C.; Drese, J. H.; Fauth, D. J.; Gray, M. L.; Qi, G. G.; Jones, C. W. Designing Adsorbents for CO_2 Capture from Flue Gas-Hyperbranched Aminosilicas Capable of Capturing CO_2 Reversibly. *J. Am. Chem. Soc.* **2008**, *130*, 2902–2903.
29. Yu, K. Q.; Sommer, W.; Weck, M.; Jones, C. W. Silica and Polymer-Tethered Pd-SCS-Pincer Complexes: Evidence for Precatalyst Decomposition to Form Soluble Catalytic Species in Mizoroki-Heck Chemistry. *J. Catal.* **2004**, *226*, 101–110.
30. Qi, X.; Yoon, H.; Lee, S. H.; Yoon, J.; Kim, S. J. Surface-Modified Imogolite by 3-APS-OsO_4 Complex: Synthesis, Characterization and Its Application in the Dihydroxylation of Olefins. *J. Ind. Eng. Chem.* **2008**, *14*, 136–141.
31. Yamamoto, K.; Otsuka, H.; Wada, S. I.; Sohn, D.; Takahara, A. Preparation and Properties of [Poly(methyl methacrylate)/Imogolite] Hybrid *via* Surface Modification Using Phosphoric Acid Ester. *Polymer* **2005**, *46*, 12386–12392.
32. Yamamoto, K.; Otsuka, H.; Wada, S.; Takahara, A. Surface Modification of Aluminosilicate Nanofiber Imogolite. *Chem. Lett.* **2001**, 1162–1163.
33. Johnson, L. M.; Pinnavaia, T. J. Hydrolysis of (Gamma-Aminopropyl) Triethoxysilane-Silylated Imogolite and Formation of A Silylated Tubular Silicate-Layered Silicate Nanocomposite. *Langmuir* **1991**, *7*, 2636–2641.
34. Johnson, L. M.; Pinnavaia, T. J. Silylation of a Tubular Aluminosilicate Polymer (Imogolite) by Reaction with Hydrolyzed (Gamma-Aminopropyl) Triethoxysilane. *Langmuir* **1990**, *6*, 307–311.
35. Bonelli, B.; Bottero, I.; Ballarini, N.; Passeri, S.; Cavani, F.; Garrone, E. IR Spectroscopic and Catalytic Characterization of the Acidity of Imogolite-Based Systems. *J. Catal.* **2009**, *264*, 15–30.
36. Ohashi, F.; Tomura, S.; Akaku, K.; Hayashi, S.; Wada, S. I. Characterization of Synthetic Imogolite Nanotubes as Gas Storage. *J. Mater. Sci.* **2004**, *39*, 1799–1801.
37. Konduri, S.; Tong, H. M.; Chempath, S.; Nair, S. Water in Single-Walled Aluminosilicate Nanotubes: Diffusion and Adsorption Properties. *J. Phys. Chem. C* **2008**, *112*, 15367–15374.
38. Mackenzie, K. J. D.; Bowden, M. E.; Brown, I. W. M.; Meinhold, R. H. Structure and Thermal Transformations of Imogolite Studied by 29Si and 27Al High-Resolution Solid-State Nuclear Magnetic-Resinance. *Clays Clay Miner.* **1989**, *37*, 317–324.
39. Wilson, M. A.; Wada, K.; Wada, S. I.; Kakuto, Y. Thermal Transformations of Synthetic Allophane and Imogolite as Revealed by Nuclear Magnetic-Resonance. *Clay Miner.* **1988**, *23*, 175–190.
40. Farmer, V. C.; Adams, M. J.; Fraser, A. R.; Palmieri, F. Synthetic Imogolite - Properties, Synthesis, and Possible Applications. *Clay Miner.* **1983**, *18*, 459–472.

41. Mass Spectra. In *NIST Chemistry WebBook*; Linstrom, P. J., Mallard, W. G., Eds.; National Institute of Standards and Technology: Gaithersburg, MD; p 20899; http://webbook.nist.gov. Accessed January 25, 2010.
42. Bronnimann, C. E.; Zeigler, R. C.; Maciel, G. E. Proton NMR-Study of Dehydration of the Silica-Gel Surface. *J. Am. Chem. Soc.* **1988**, *110*, 2023–2026.
43. Liu, C. H. C.; Maciel, G. E. The Fumed Silica Surface: A Study by NMR. *J. Am. Chem. Soc.* **1996**, *118*, 5103–5119.
44. Trebosc, J.; Wiench, J. W.; Huh, S.; Lin, V. S. Y.; Pruski, M. Solid-State NMR Study of MCM-41-type Mesoporous Silica Nanoparticles. *J. Am. Chem. Soc.* **2005**, *127*, 3057–3068.
45. Eckert, H.; Yesinowski, J. P.; Silver, L. A.; Stolper, E. M. Water in Silicate-Glasses - Quantitation and Structural Studies by 1H Solid Echo and MAS-NMR Methods. *J. Phys. Chem.* **1988**, *92*, 2055–2064.
46. Yesinowski, J. P.; Eckert, H.; Rossman, G. R. Characterizaiton of Hydrous Species in Minerals by High-Speed 1H MAS NMR. *J. Am. Chem. Soc.* **1988**, *110*, 1367–1375.
47. Vega, A. J.; Scherer, G. W. Study of Structural Evolution of Silica-Gel Using 1H and 29Si NMR. *J. Non-Cryst. Solids* **1989**, *111*, 153–166.
48. Leisen, J.; Beckham, H. W.; Benham, M. Sorption Isotherm Measurements by NMR. *Solid State Nucl. Magn. Reson.* **2002**, *22*, 409–422.
49. Laws, D. D.; Bitter, H. M. L.; Jerschow, A. Solid-state NMR Spectroscopic Methods in Chemistry. *Angew.Chem., Int. Ed.* **2002**, *41*, 3096–3129.
50. Goodman, B. A.; Russell, J. D.; Montez, B.; Oldfield, E.; Kirkpatrick, R. J. Structural Studies of Imogolite and Allophanes by Aluminum-27 and Silicon-29 Nuclear Magnetic Resonance Spectroscopy. *Phys. Chem. Miner.* **1985**, *12*, 342–346.
51. Wada, S. I.; Wada, K. Density and Structure of Allophane. *Clay Miner.* **1977**, *12*, 289–298.
52. Abidin, Z.; Matsue, N.; Henmi, T. Differential Formation of Allophane and Imogolite: Experimental and Molecular Orbital Study. *J. Comput.-Aided Mater. Des.* **2007**, *14*, 5–18.
53. Lippmaa, E.; Magi, M.; Samoson, A.; Engelhardt, G.; Grimmer, A. R. Structural Studies of Silicates by Solid-State High-Resolution 29Si NMR. *J. Am. Chem. Soc.* **1980**, *102*, 4889–4893.
54. Merzbacher, C. I.; McGrath, K. J.; Higby, P. L. 29Si NMR and Infrared Reflectance Spectroscopy of Low-Silica Calcium Aluminosilicate Glasses. *J. Non-Cryst. Solids* **1991**, *136*, 249–259.
55. Akitt, J. W. Multinuclear Studies of Aluminum Compounds. *Prog. Nucl. Magn. Reson. Spectrosc.* **1989**, *21*, 1–149.
56. Gilson, J. P.; Edwards, G. C.; Peters, A. W.; Rajagopalan, K.; Wormsbecher, R. F.; Roberie, T. G.; Shatlock, M. P. Pentacoordinated Aluminum in Zeolites and Aluminosilicates. *J. Chem. Soc. Chem. Commun.* **1987**, 91–92.
57. Haddix, G. W.; Narayana, M.; Gillespie, W. D.; Georgellis, M. B.; Wu, Y. Double-Rotation and Magic-Angle-Spinning NMR-Study of an Ultrastable Y-Zeolite. *J. Am. Chem. Soc.* **1994**, *116*, 672–674.
58. Schmucker, M.; MacKenzie, K. J. D.; Schneider, H.; Meinhold, R. NMR Studies on Rapidly Solidified SiO_2-Al_2O_3 and SiO_2-Al_2O_3-Na_2O-Glasses. *J. Non-Cryst. Solids* **1997**, *217*, 99–105.
59. Farnan, I.; Dupree, R.; Forty, A. J.; Jeong, Y. S.; Thompson, G. E.; Wood, G. C.; Structural Information about Amorphous Anodic Alumina from 27Al MAS, N. M. R. *Philos. Mag. Lett.* **1989**, *59*, 189–195.
60. IngramJones, V. J.; Slade, R. C. T.; Davies, T. W.; Southern, J. C.; Salvador, S. Dehydroxylation sequences of gibbsite and boehmite: Study of differences between soak and flash calcination and of particle-size effects. *J. Mater. Chem.* **1996**, *6*, 73–79.
61. Mackenzie, K. J. D.; Brown, I. W. M.; Meinhold, R. H.; Bowden, M. E. Thermal-Reactions oF Pyrophyllite Studied by High-Resolution Solid-State 27Al and 29Si Nuclear Magnetic-Resonance Spectroscopy. *J. Am. Ceram. Soc.* **1985**, *68*, 266–272.
62. Luan, Z. H.; Cheng, C. F.; He, H. Y.; Klinowski, J. Thermal-Stability of Structural Aluminum in the Mesoporous Molecular-Sieve MCM-41. *J. Phys. Chem.* **1995**, *99*, 10590–10593.
63. Man, P. P.; Klinowski, J.; Trokiner, A.; Zanni, H.; Papon, P. Selective and Non-Selective NMR Excitation of Quadrupolar Nuclei in the Solid-State. *Chem. Phys. Lett.* **1988**, *151*, 143–150.
64. Sing, K. S. W.; Everett, D. H.; Haul, R. A. W.; Moscou, L.; Pierotti, R. A.; Rouquerol, J.; Siemieniewska, T. Reporting Physisorption Data for Gas Solid Systems with Special Reference to the Determination of Surface-Area and Porosity (Recommendations 1984). *Pure Appl. Chem.* **1985**, *57*, 603–619.
65. Creton, B.; Bougeard, D.; Smirnov, K. S.; Guilment, J.; Poncelet, O. Molecular Dynamics Study of Hydrated Imogolite. 1. Vibrational Dynamics of the Nanotube. *J. Phys. Chem. C* **2008**, *112*, 10013–10020.
66. Guimaraes, L.; Enyashin, A. N.; Frenzel, J.; Heine, T.; Duarte, H. A.; Seifert, G. Imogolite Nanotubes: Stability, Electronic, and Mechanical Properties. *ACS Nano* **2007**, *1*, 362–368.
67. Alvarez-Ramirez, F. Ab initio Simulation of the Structural and Electronic Properties of Aluminosilicate and Aluminogermanate Natotubes with Imogolite-like Structure. *Phys. Rev. B: Condens. Matter Mater. Phys.* **2007**, 76.
68. Zang, J.; Konduri, S.; Nair, S.; Sholl, D. S. Self-Diffusion of Water and Simple Alcohols in Single-Walled Aluminosilicate Nanotubes. *ACS Nano* **2009**, *3*, 1548–1556.
69. Hoshino, H.; Urakawa, H.; Donkai, N.; Kajiwara, K. Simulation of Mesophase Formation of Rodlike Molecule, Imogolite. *Polym. Bull.* **1996**, *36*, 257–264.
70. Konduri, S.; Mukherjee, S.; Nair, S. Strain Energy Minimum and Vibrational Properties of Single-Walled Aluminosilicate Nanotubes. *Phys. Rev. B: Condens. Matter Mater. Phys.* **2006**, 74.
71. Zhao, M. W.; Xia, Y. Y.; Mei, L. M. Energetic Minimum Structures of Imogolite Nanotubes: A First-Principles Prediction. *J. Phys. Chem. C* **2009**, *113*, 14834–14837.
72. Cambedouzou, J.; Pichot, V.; Rols, S.; Launois, P.; Petit, P.; Klement, R.; Kataura, H.; Almairac, R. On the Diffraction Pattern of C_{60} Peapods. *Eur. Phys. J. B* **2004**, *42*, 31–45.
73. Kawasaki, S.; Hara, T.; Yokomae, T.; Okino, F.; Touhara, H.; Kataura, H.; Watanuki, T.; Ohishi, Y. Pressure-Polymerization of C_{60} Molecules in a Carbon Nanotube. *Chem. Phys. Lett.* **2006**, *418*, 260–263.
74. Kawasaki, S.; Matsuoka, Y.; Yokomae, T.; Nojima, Y.; Okino, F.; Touhara, H.; Kataura, H. XRD and TEM Study of High Pressure Treated Single-Walled Carbon Nanotubes and C_{60}-Peapods. *Carbon* **2005**, *43*, 37–45.